Atomic and electronic structures of superconducting BaFe_{2}As_{2}/SrTiO_{3} superlattices

P. Gao, Y. Zhang, S. Y. Zhang, S. Lee, J. Weiss, J. R. Jokisaari, E. E. Hellstrom, D. C. Larbalestier, C. B. Eom, and X. Q. Pan

Atomic and Electronic Structures of Superconducting

BaFe$_2$As$_2$/SrTiO$_3$ Superlattices

Peng Gao[1†], Yi Zhang[1,2], Shuyi Zhang[1,2], Sanghan Lee[3†], Jeremy D. Weiss[4], Jacob R. Jokisaari[1], Eric E. Hellstrom[4], David C. Larbalestier[4], Chang-Beom Eom[3], and Xiaoqing Pan[1*†]

[1]Department of Materials Science and Engineering, University of Michigan, Ann Arbor, Michigan 48109, USA

[2]National Laboratory of Solid State Microstructures and Department of Materials Science and Engineering, Nanjing University, Nanjing, 210093, P.R. China

[3]Department of Materials Science and Engineering, University of Wisconsin-Madison, Madison, WI 53706, USA

[4]Applied Superconductivity Center, National High Magnetic Field Laboratory, Florida State University, 2031 East Paul Dirac Drive, Tallahassee, FL 32310, USA

†Current affiliation: School of Physics, Peking University, Beijing100871, China (P.G.). School of Materials Science and Engineering, Gwangju Institute of Science and Technology, Gwangju 500-712, Republic of Korea (S.L.). Department of Chemical Engineering and Materials Science and Department of Physics and Astronomy, University of California - Irvine, Irvine, CA 92697 (X.Q.P.)

* Corresponding author: panx@umich.edu

ABSTRACT: The nanoscale structural, chemical and electronic properties of artificial engineered superlattice thin films consisting of superconducting Co-doped BaFe$_2$As$_2$ (Ba-122) and non-superconducting SrTiO$_3$ (STO) layers are determined

by using atomically resolved scanning transmission electron microscopy and electron energy loss spectroscopy. The bonding of Ba-122/STO occurring between As (Ba) and SrO (TiO$_2$) terminated layers has been identified. The thin STO (3 unit-cell) insertion layers are mixture of cations (Ba, Sr, Fe and Ti) and rich in oxygen vacancies and the Ba-122 layers (10 unit-cell) are free of vertical second phases. Our results explain why these supperlattices show anisotropic transport response to external magnetic field, i.e., strong *ab*-axis pinning (enhancing critical current density) and no *c*-axis pinning, which is opposite to single layer Ba-122 thin film. These findings reveal physical and chemical properties of superconducting/non-superconducting hetero-structures and provide important insights into engineering of superconducting devices.

High quality epitaxial heterostructures consisting of superconducting and non-superconducting layers have been attracted extensive research interest because their novel properties make them very attractive candidates for a variety of applications, such as Josephson junctions, superconducting quantum interference device (SQUID) and other field-effect devices [1-7]. Epitaxial pnictide thin films, however, have so far been hard to produce due to the volatile elements in the iron-based superconductor phase and therefore it is difficult to control the stoichiometry of the deposited films [8,9]. By employing epitaxial SrTiO$_3$ (STO) templates, we were able to grow high quality epitaxial Co-doped

BaFe$_2$As$_2$ (Ba-122) thin films on (La,Sr)(Al,Ta)O$_3$ (LSAT) substrates [10-12]. Recently, we reported the growth and properties of artificially engineered superlattices of Co-doped BaFe$_2$As$_2$/SrTiO$_3$ (Ba-122/STO) and Co-doped BaFe$_2$As$_2$/undoped BaFe$_2$As$_2$ [12] . The former was possible due to their similar structures of which bulk Ba-122 has a tetragonal structure with lattice parameter a=3.962 Å, c=13.017 Å [13,14], while cubic STO has a lattice parameter with a= 3.905 Å. As a result of small misfit (1.4%) at the interface, the films showed excellent epitaxial growth with the use of the oxide templates.

Previously we reported that single layer Ba-122 thin films showed strong c-axis pinning effect which enhances the in-field performance of the critical current density [10,11]. High resolution TEM results indicated that the presence of the c-axis aligned self-assembled oxide nanopillars in Ba-122 thin film [15] accounts for the c-axis pinning effect. In contrast, superlattice structure of Ba-122/STO shows very strong ab-axis pinning rather than c-axis pinning. The different transport properties in these thin film devices essentially originate from the nature of defects, i.e., heterointerfaces and second phases. Precise knowledge of what the atomic and electronic structures of heterointerfaces and second phases are and how the second phases distribute in these thin films, therefore, is a key prerequisite to understand the physics of superconducting/oxide heterostructures and subsequently develop superconductor devices. However, the defects' properties are difficult to extract from the bulk-based measurement techniques (e.g., X-ray diffraction and electrical-based measurements) because the defects (e.g., interfaces, second phases) are typically in atomic- or nano- size and their properties can significantly change from unit cell to unit cell. In this letter, the state of art of aberration-corrected scanning transmission electron microscopy (STEM) combining with electron energy loss

spectroscopy (EELS) with sub-Angstro m spatial resolution are employed to enable nanosized structure, composition, and chemical states of defects in Ba-122/STO superlattice to be determinate and therefore to reveal the underlying mechanism of anisotropic electromagnetic transport properties. The bonding of Ba-122/STO heterostructure is found to occur between an As (Ba) and a SrO (TiO_2) terminated layers. All the Ba-122 layers are single crystal without any other phases. Free of second phases in Ba-122 layers can be attributed to the presence of STO insertion layers which act as nuclei for other perovskite-related second phases (e.g. Ba-Fe-O) as the quantitative electron energy loss spectroscopy (EELS) analysis indicates a mixture of cations of Ba, Sr, Fe and Ti in these insertion layers. Meanwhile oxygen vacancies and Ti^{3+} ions are found in the STO layers. Based on these findings, we conclude that the elimination of *c*-axis pinning effect in such a structure results from absent of vertical defects in each Ba-122 layers, while the *ab*-axis pinning accounts for the inherent defects induced by the insertion of non-superconducting STO layers.

Single-crystal Co-doped Ba-122 and STO superlattice were grown by pulsed laser deposition (PLD) on (La;Sr)(Al;Ta)O_3 (LSAT) substrates [10,16]. The details of the growth and electromagnetic properties were reported elsewhere [12]. The superconducting transition temperatures of these structures vary from 17.0 to 19.7 K with small transition width ΔTc: 1.1~2.0 K. These structures were characterized by using aberration-corrected scanning TEMs (JEOL 2100F and JEOL ARM200) operated at 200 kV with probe size of 0.08 nm. High angle annular dark field (HAADF) images allowed high atomic number features such as the Ba, Sr, As, Fe and TiO columns to be directly distinguished and therefore are used to determine atomic bonding at the interfaces.

4

Electron energy loss spectroscopy (EELS) was employed to probe the local chemistry of the heterostructures at the atomic scale. Fig. 1a shows a cross sectional HAADF image of 24-layer Ba-122/STO structure with total thickness of ~320 nm. The first template STO layer on LSAT is ~40 nm thick (100 unit cells). A higher resolution HAADF image (Fig. 1b) seen along the <100> direction shows that each STO layer is 3 unit cells thick, and Ba-122 has a thickness of 10 unit cells.

Fig. 2a shows a typical high magnification HAADF image of the interfacial region of the first Ba-122 thin film on the STO template layer. Each atom columns can be distinguished directly as the intensity in HAADF image (Z-contrast) is sensitive to the atomic number. The intensity of A-site cations (in ABO_3 perovskite structure) in layers 'B', 'C', 'D', 'E' and 'F' are obviously higher than that in layers below 'A' which is supposed to be Sr, indicating mixture of Sr and heavier Ba atoms within the STO template layer underneath the interface. The substitution of Sr by Ba should gradually decrease from the interface to deeper interior of STO template layer. The intensities in the layers 'E' and 'F', however, are abnormally lower than that of the layer 'D'. This can be explained by that the intensity in HAADF image is also very sensitive to the distances between atom columns and the space between 'E' and 'F' is ~1.37 times of that between layer 'D' and 'E' calculated by two dimensional Gaussian fitting Sr/Ba columns (in Fig. 2b). Weaker bonding also occurs in the first Ba-122 layer near interface, where the distance between layer 'F' and layer 'G' is 1.06 times of that between layer 'G' and 'H' (Fig. 2b).

In the STO insertion layer, the mixture of A-site cations also occurs as shown in Fig. 2c where the intensity of layer 'K', 'L', 'M' and 'N' are not homogenous and therefore

pure Ba or Sr columns can be ruled out (the co-existing Ba and Sr is also evidenced by X-ray dispersive spectra shown in Fig. S1). The intensity ratios of A-site columns in the inserted STO ('K', 'L', 'M' and 'N') layers to Ba layer ('O') are ~0.80-0.87 compared to the ratio of layer 'A' (Sr column) to layer 'G' (Ba column) ~0.64 in Fig. 2a, indicating heavy substitution of Sr by Ba atoms in these insertion layers. The lattice ratio of c/a in these insertion layers remains to be ~1 within experimental error (Fig. 2d). Although BTO and STO have different lattice constants (~3% mismatch), heavy doping in these insertion layers doesn't cause obvious structure distortion and no dislocations are observed in the films.

The bonding between the Ba-122 and perovskite STO can be determined directly as shown in Fig. 2e. The As layer in Ba-122 bonds to a SrO layer or the Ba layer bonds to TiO_2 layer depending on what the surface layer is in pristine STO before deposition of Ba-122. The simulated HAADF image of Ba-122 structure (right inset of Fig.2e) shows a good agreement with the experimental image. The distance between Fe and As atoms is ~1.35 Å based on the structure model and these atoms are readily distinguishable from the HAADF image (Fig. 2f).

To get the distribution of elements, the spatial variation of EELS spectra across a STO insertion layer, a Ba-122 layer and interface of a Ba-122/STO template layer are acquired (in Fig. 3a) with spatial step size of 0.09 nm. At the interface of the Ba-122/STO template layer, Ba atoms diffuse into the STO layer with a depth of ~1.5 nm (Fig. 3a), which is consistent with ~ 4 unit cells of mixed cations in Fig. 2a. In contrast, diffusion of Fe atoms is much shorter. The quantitative EELS analysis determined from the ratios of integrated intensities of Ti-L, Fe-L and Ba-M edges (in Fig. 3b) indicates the Fe/Ba ratio

6

in the Ba-122 layer is ~1.91 that is very close to the stoichiometric proportion within experimental error. Within the STO insertion layer, both Ba and Fe signals are strong, and the Fe/Ba ratio is close to 1.

In our previous work, the second phases of $BaFeO_2$ nanopillars were observed in single Co-doped Ba-122 thin films [15] because oxygen was present in surroundings from targets and the chamber walls and therefore the second phases formed easily due to the intrinsic similarities in the structure and chemistry of $BaFeO_2$ and STO. For the superlattice films in this work, in addition to the cation substitution, it is also possible that other perovskite-related phases Ba-Fe-O nucleated within the STO layers to form a mixture. In the STO layer, the ratio of Fe:Ti calculated from the EELS is close to 1:1 and EDS shows the Sr:Ti also approximately equals to 1:1 (Supporting information Fig. S1). In other words, the insertion STO layer can be expressed as $(Ba_{0.5}Sr_{0.5})(Fe_{0.5}Ti_{0.5})O_{3-x}$ (x denotes oxygen deficiency). In this case, the concentration of Ba in this insertion layer is 0.5 atom per unit cell with volume of a^3 (a= 3.905 Å for bulk). This value is close to that in a single crystal Ba-122 layer, which is 2 atoms in a^2c (a= 3.962 Å and c=13.017 Å for bulk). As a result, across the insertion layer the counts of Ba remain no obvious change, but the counts of Fe are reduced to half from the EELS line scan (Fig. 3a and b). The mixture of cations, however, is not homogeneous in these insertion layers as spectra acquired from different locations show that the ratio of Fe:Ti varies from 0.6:1 to 1:1.

In order to see the detailed electronic structures of superconducting/non-superconducting interfaces, fine structures of Ti-$L_{2,3}$ and O-K edges acquired simultaneously from different locations are plotted in Figure 4a, b. Spectra 1-3 were taken in the middle of insertion STO layer, 2 unit cells underneath the interface of Ba-

122/STO template layer and 7 unit cells from the interface, individually. Fig. 4a shows the fine structure of O-K edge that is sensitive to the concentration of oxygen vacancies. The decrease in the intensities of the peaks (indicated by arrows) in spectrum 1 and 2 is a clear manifestation of oxygen vacancies existing in these regions [17-19]. Additionally, the Ti-L (Ti $2p$ to $3d$) core edges are also sensitive to a change in valence of Ti [20]. Peaks in the Ti-L$_{2,3}$ edges become broader both in the insertion layer (in spectrum 1) and near the interface (in spectrum 2) with peak splitting becoming less pronounced. This broadening results from the existence of Ti^{3+} ions [17,18]. Furthermore, these peaks in spectrum 1 and 2 are slightly shifted to lower energy compared to spectrum 3, which is another characteristic of Ti^{3+}.

We have profiled the distribution of Ti^{3+} and Ti^{4+} across the interfaces, as shown in Fig. 4c. The relative composition of Ti^{3+} and Ti^{4+} has been extracted by fitting the Ti-L edges using reference spectra of Ti^{3+} (acquired from LaTiO$_3$) and Ti^{4+} (acquired from SrTiO$_3$) that were obtained under the same experimental conditions. A high concentration of Ti^{3+} is observed within the STO insertion layer and underneath the interface of the Ba-122/STO template layer. The presence of Ti^{3+} underneath the surface of STO template layer is reasonable because before growing Ba-122 oxygen vacancies have already formed at the surface of STO where oxygen anions are very active to be released due to asymmetric interaction with cations, especially in the vacuum chamber at high temperature. In the inserted STO layers, the Ti/O ratio is calculated to be ~1/2.75 in this region since the population of Ti^{3+} approximately equals to that of Ti^{4+}. With the perovskite structure, STO remains stable even though a large population of oxygen vacancies exists. The high concentration of oxygen vacancies in the inserted STO layer

8

results from the fact that the Ba and Fe ions take oxygen anions from the STO phase to form a mixture of perovskite-related second phases. In these insertion layers, most of Fe ions are Fe^{2+} based on EELS analysis (Supporting information Fig. S2) [21,22]. $SrTiO_{3-x}$, $BaTiO_{3-y}$ $BaFeO_2$ and $SrFeO_2$ (x and y denote oxygen deficiency), therefore, are the most likely candidates comprising the mixture of insertion layers.

In summary, the atomic bonding of a structurally modulated superconducting and non-superconducting Ba-122/STO superlattice with atomically sharp interface is determined by Z-contrast images with sub-Å resolution: the As (Ba) layer in tetragonal Ba-122 bonds to the SrO (TiO_2) layer of perovskite STO. Substitution of Sr by Ba atoms occurs both in the thin STO insertion layers of the superlattice and underneath the interface of the Ba-122 and STO template layer. The quantitative EELS analysis indicates that the STO insertion layers is a mixture of perovskite phases and consists of a large population of oxygen vacancies. These findings provide a complete understanding of the anisotropic transport properties of these structures: the *ab*-axis pinning stems from layered but inherent non-superconducting STO structures, while vertical-defect-free Ba-122 layers account for elimination of *c*-axis pinning as the non-superconducting phases are concentrated in the STO insertion layers.

Reference

[1]   B. D. Josephson, Physics Letters **1**, 251 (1962).
[2]   R. C. Jaklevic, A. H. Silver, J. Lambe, and J. E. Mercereau, Phys. Rev. Lett. **12**, 159 (1964).
[3]   U. Poppe, P. Prieto, J. Schubert, H. Soltner, K. Urban, and C. Buchal, Solid State Commun. **71**, 569 (1989).
[4]   J. Gao, W. A. M. Aarnink, G. J. Gerritsma, and H. Rogalla, Physica C **171**, 126 (1990).
[5]   X. X. Xi, C. Doughty, A. Walkenhorst, C. Kwon, Q. Li, and T. Venkatesan, Phys. Rev. Lett. **68**, 1240 (1992).
[6]   X. D. Wu, S. R. Foltyn, R. C. Dye, Y. Coulter, and R. E. Muenchausen, Appl. Phys. Lett. **62**, 2434 (1993).
[7]   A. T. Bollinger, G. Dubuis, J. Yoon, D. Pavuna, J. Misewich, and I. Bozovic, Nature **472**, 458 (2011).
[8]   S. Haindl, M. Kidszun, A. Kauffmann, K. Nenkov, N. Kozlova, J. Freudenberger, T. Thersleff, auml, J. nisch, J. Werner, E. Reich, L. Schultz, and B. Holzapfel, Phys. Rev. Lett. **104**, 077001 (2010).
[9]   H. Hiramatsu, T. Katase, T. Kamiya, M. Hirano, and H. Hosono, Appl. Phys. Lett. **93**, 162504 (2008).
[10]   S. Lee, J. Jiang, Y. Zhang, C. W. Bark, J. D. Weiss, C. Tarantini, C. T. Nelson, H. W. Jang, C. M. Folkman, S. H. Baek, A. Polyanskii, D. Abraimov, A. Yamamoto, J. W. Park, X. Q. Pan, E. E. Hellstrom, D. C. Larbalestier, and C. B. Eom, Nature Materials **9**, 397 (2010).
[11]   C. Tarantini, S. Lee, Y. Zhang, J. Jiang, C. W. Bark, J. D. Weiss, A. Polyanskii, C. T. Nelson, H. W. Jang, C. M. Folkman, S. H. Baek, X. Q. Pan, A. Gurevich, E. E. Hellstrom, C. B. Eom, and D. C. Larbalestier, Appl. Phys. Lett. **96**, 142510 (2010).
[12]   S. Lee, C. Tarantini, P. Gao, J. Jiang, J. D. Weiss, F. Kametani, C. M. Folkman, Y. Zhang, X. Q. Pan, E. E. Hellstrom, D. C. Larbalestier, and C. B. Eom, Nature Materials **12**, 392 (2013).
[13]   Q. Huang, Y. Qiu, W. Bao, M. A. Green, J. W. Lynn, Y. C. Gasparovic, T. Wu, G. Wu, and X. H. Chen, Phys. Rev. Lett. **101**, 257003 (2008).
[14]   M. Rotter, M. Tegel, D. Johrendt, I. Schellenberg, W. Hermes, and R. Pottgen, Physical Review B **78**, 020503 (2008).
[15]   Y. Zhang, C. T. Nelson, S. Lee, J. Jiang, C. W. Bark, J. D. Weiss, C. Tarantini, C. M. Folkman, S.-H. Baek, E. E. Hellstrom, D. C. Larbalestier, C.-B. Eom, and X. Pan, Appl. Phys. Lett. **98**, 042509 (2011).
[16]   S. Lee, J. Jiang, J. D. Weiss, C. M. Folkman, C. W. Bark, C. Tarantini, A. Xu, D. Abraimov, A. Polyanskii, C. T. Nelson, Y. Zhang, S. H. Baek, H. W. Jang, A. Yamamoto, F. Kametani, X. Q. Pan, E. E. Hellstrom, A. Gurevich, C. B. Eom, and D. C. Larbalestier, Appl. Phys. Lett. **95**, 212505 (2009).
[17]   D. A. Muller, N. Nakagawa, A. Ohtomo, J. L. Grazul, and H. Y. Hwang, Nature **430**, 657 (2004).
[18]   A. Ohtomo, D. A. Muller, J. L. Grazul, and H. Y. Hwang, Nature **419**, 378 (2002).

[19]   N. Reyren, S. Thiel, A. D. Caviglia, L. F. Kourkoutis, G. Hammerl, C. Richter, C. W. Schneider, T. Kopp, A. S. Ruetschi, D. Jaccard, M. Gabay, D. A. Muller, J. M. Triscone, and J. Mannhart, Science **317**, 1196 (2007).
[20]   M. Sankararaman and D. Perry, Journal of Materials Science **27**, 2731 (1992).
[21]   P. A. van Aken and B. Liebscher, Physics and Chemistry of Minerals **29**, 188 (2002).
[22]   P. M. Aswathy, J. B. Anooja, P. M. Sarun, and U. Syamaprasad, Superconductor Science & Technology **23**, 073001 (2010).

Figures and captions:
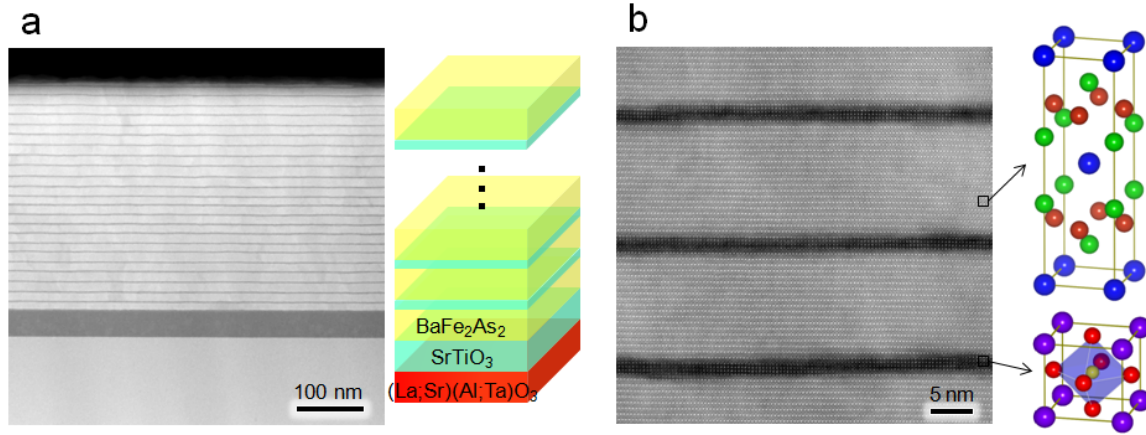
FIG. 1 (a) HAADF image of 24 layers of Ba-122/STO superlattice on LSAT substrate with 40 nm STO template layer. A schematic is shown in the right of image. (b) High resolution HAADF image of the <100> projection of Ba-122/STO structure with 10 unit cells in each Ba-122 layer and 3 unit cells in each STO layer. A schematic of Ba-122 and STO structures is included to the right of images. Blue atoms: Ba. Purple: Sr; Green: As; Brown: Fe; Red: oxygen.
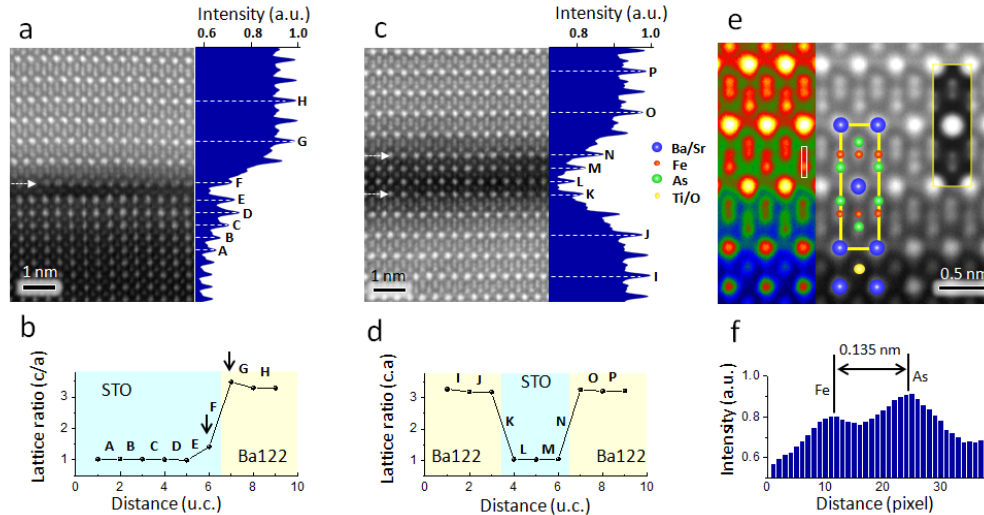

FIG. 2 (a) HAADF image of the interface between the first Ba-122 layer and STO template layer. The interface of Ba-122/STO is indicated by the arrow. Near the interface in STO, inhomogeneous intensities in the profile indicate mixture of Sr and Ba atoms. (b) The c/a ratio across the interface. The calculation is based on Ba/Sr atoms positions from the HAADF image which is averaged along the interface (horizontally) to reduce noise. Atom positions were determined by simultaneously fitting two dimensional Gaussian peaks. The arrows indicate the weak bonding at the interface. (c) HAADF image of

13

interfaces of Ba-122 layer and 3 unit cells STO insertion layer. The interfaces of Ba-122/STO are indicated by the arrows. In the insertion layer, inhomogeneous intensities in the profile indicate mixture of Sr and Ba atoms. (d) The c/a ratio across the insertion layer calculated from Ba/Sr positions in the average HAADF image. (e) Enlarged view of the Ba-122/STO interface structure from an averaged image. Left: color-scale highlights each atom columns. Middle: the atomic schematic structure overlaid on the image. Right: the simulated HAADF image by the Mactempas software. (f) The intensity profile from the rectangular region in (e) distinguishes the Fe and As atom columns.
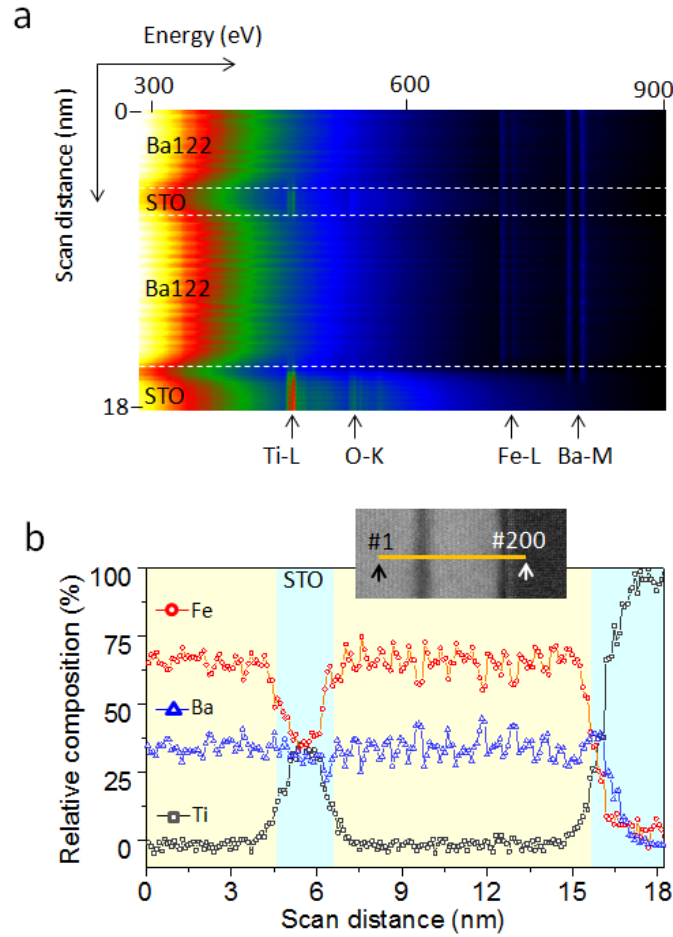

FIG. 3 (a) EELS line scan across a STO insertion layer, a Ba-122 layer and interface of a Ba-122/STO template layer with step of ~0.09 nm. Ba diffusion in STO template layer is much deeper than that of Fe. In the STO insertion layer, the intensity of Fe decreases, but intensity of Ba does not show obvious change. (b) Relative composition extracted from EELS line-scan show the Fe:Ba ratio is close to 1.91 in the Ba-122 and Ba:Fe:Ti ratio is close to 1:1:1 in the middle of insertion STO layer.
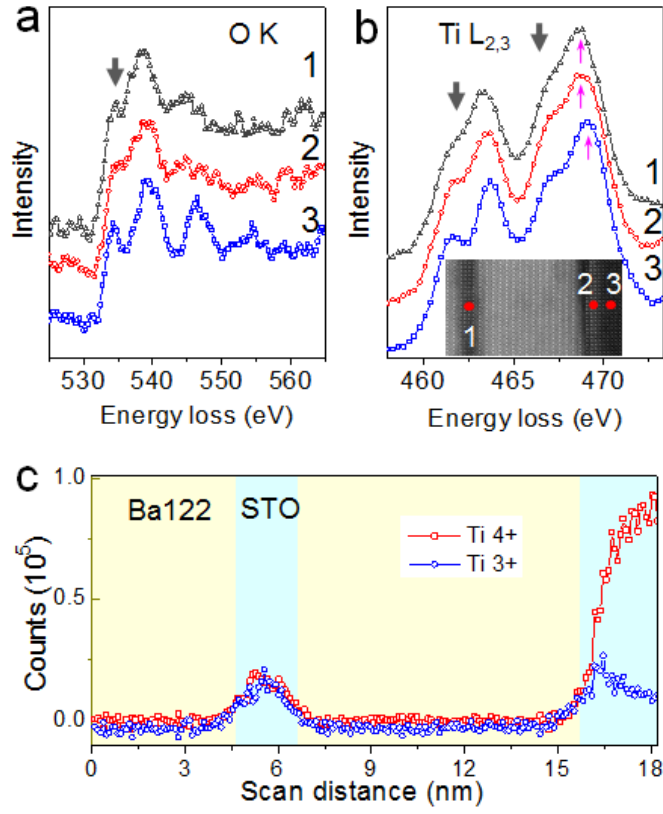
14

FIG. 4. (a) Fine structure of O-K edges showing the presence of oxygen vacancies in regions 1 and 2. (b) Fine structure of Ti-L edges shows some reduction of Ti^{4+} to Ti^{3+} in regions 1 and 2. The insert shows the locations where the spectra were acquired. (c) Distribution of Ti^{3+} and Ti^{4+} by fitting Ti-L edges using reference spectra of Ti^{4+} in $SrTiO_3$ and Ti^{3+} in $LaTiO_3$.